Journal of Biomedical Optics

BiomedicalOptics.SPIEDigitalLibrary.org

Ultrahigh polarimetric image contrast enhancement for skin cancer diagnosis using InN plasmonic nanoparticles in the terahertz range

Michael Ney
Ibrahim Abdulhalim

SPIE.

Ultrahigh polarimetric image contrast enhancement for skin cancer diagnosis using InN plasmonic nanoparticles in the terahertz range

Michael Ney* **and Ibrahim Abdulhalim**
Ben-Gurion University of the Negev, Departement of Electro-Optics Engineering and the Ilse-Katz Institute for Nanoscale Sceince and Technology, P.O. Box 653, Beer-Sheva 8410501, Israel

Abstract. Mueller matrix imaging sensitivity, to delicate water content changes in tissue associated with early stages of skin cancer, is demonstrated by numerical modeling to be enhanced by localized surface plasmon resonance (LSPR) effects at the terahertz (THz) range when InN nanoparticles (NPs) coated with Parylene-C are introduced into the skin. A skin tissue model tailored for THz wavelengths is established for a Monte Carlo simulation of polarized light propagation and scattering, and a comparative study based on simulated Mueller matrices is presented considering different NPs' parameters and insertion into the skin methods. The insertion of NPs presenting LSPR in the THz is demonstrated to enable the application of polarization-based sample characterization techniques adopted from the scattering dominated visible wavelengths domain for the, otherwise, relatively low scattering THz domain, where such approach is irrelevant without the NPs. Through these Mueller polarimetry techniques, the detection of water content variations in the tissue is made possible and with high sensitivity. This study yields a limit of detection down to 0.0018% for relative changes in the water content based on linear degree of polarization—an improvement of an order of magnitude relative to the limit of detection without NPs calculated in a previous ellipsometric study. [DOI: 10.1117/1.JBO.20.12.125007]

Keywords: biomedical optics; Monte Carlo simulations; scattering; polarimetry; millimeter waves.

Paper 150425R received Jun. 23, 2015; accepted for publication Nov. 24, 2015; published online Dec. 24, 2015.

1 Introduction

The development of high sensitivity noninvasive optical sensing techniques for early detection of skin tissue abnormalities, such as various skin cancer types, has been the subject of extensive academic and commercial activities during the past decades.[1–20] A variety of methods have been examined for this goal, each of them tailored around some optical mechanism providing it with certain ability to discriminate abnormal from healthy tissue. One example is imaging at terahertz (THz) wavelengths that suffer less from scattering effects, can have longer tissue penetration depth (0.5 to 6.5 mm depending on water content of the tissue[21]) compared with visible wavelengths (~1 mm[22]) and present sensitivity to local water content in the tissue shaping the reflected electromagnetic (EM) field. The reflected field intensity image can, therefore, provide contrast-based discrimination of healthy and nonhealthy tissue by associating local intensity changes to localized elevated levels of water content indicating pathology, as it is well established that skin cancer causes elevated water content.[6–14] With the previously mentioned benefits of THz radiation-based biosensing and imaging for skin cancer detection, it is important to mention a key downside of imaging with long wavelengths which is the reduced imaging resolution relative to the near-infrared (NIR) and visible (VIS) spectral domain traditional optical imaging, as THz imaging enables normally resolution of a few hundreds of microns. However, in recent years, growth of interest in the field of THz advances has already been made in this area. Recent studies have yielded both more effective THz sources and imaging techniques enabling subwavelength resolution THz imaging techniques by reducing the spatial size of the THz sources' beam, which can provide resolutions from several tens of microns[23] to several hundreds of nanometers,[24] which should be more than sufficient for early skin cancer detection via contrast-based imaging.

Another class of sensing techniques is based on localized surface plasmon resonance (LSPR) methods, commonly implemented for biomedical sensing at the visible and near-visible spectral domain using gold and silver nanoparticles (NPs).[15] LSPR is known for sensitivity enhancement for various sensing configurations due to the spectrally and spatially localized enhancement of the EM field near the NPs in the tissue, resulting in high sensitivity to local changes in the permittivity near the NPs. This sensitivity is used for "sniffing" local changes in the tissue related to pathological processes.

A third class of imaging and sensing techniques is polarized light imaging, mostly developed in the visible and NIR frequencies, that can provide higher sensitivity,[1–5,16,19,20,25] better healthy/unhealthy tissue contrast,[2,5] and imaging of subsurface structures in the tissue[26–28] when compared with nonpolarized or single polarization imaging. These NIR and visible frequencies polarimetric techniques lean mostly on the detection of skin tissue pathologies based on scattering-induced effects such as alteration of tissue cells and organelles sizes and orientation/order due to the development of cancer. The basis for these techniques is usually a creation of artificial images with improved contrast between elevated normal/abnormal tissue regions,

*Address all correspondence to: Michael Ney, E-mail: ney@post.bgu.ac.il

1083-3668/2015/$25.00 © 2015 SPIE

instead of the regular intensity images having low contrast. These improved contrast images are actually polarimetric images sensitive to tissue alterations associated with cancer such as Mueller–Jones matrix images or other polarimetric parameters images based on combinations of the latter. Although impressive performance of each of these methods has already been demonstrated, improving measurement sensitivity and reliability of these diagnosis methods is still needed.

In this work, we propose improving the THz imaging detection sensitivity of skin cancer and healthy/abnormal tissue contrast by combining the advantages of THz imaging, polarized light imaging, and LSPR. This combination of methods is made possible by considering a new type of spherical NPs made from InN, a material presenting LSPR at the THz domain. Although InN has been used for surface plasmon resonance-based sensing techniques,[29–31] it has not been considered, to the best of our knowledge, as a material for LSPR-based biosensing for skin cancer detection in the form of NPs. We demonstrate the expected improvement in sensitivity for polarized light-based detection of changes in tissue water content at the THz as a result of seeding the skin tissue with InN-based NPs, and estimate the improved limit of detection for very small water content changes associated with the early stages of development of the disease. A discussion regarding the desired spherical NPs parameters, such as the material, radii, biocompatibility, and concentration, is presented along with a consideration of two different NPs insertion into the tissue techniques. Optimal NP parameters and insertion technique are then suggested.

The assessment of the EM response and sensitivity analysis for the proposed diagnosis method has been performed using a Monte Carlo (MC) simulation for polarized light propagation in skin tissue embedded with NPs. Such simulations have been widely demonstrated to provide accurate predictions for the behavior of reflected and transmitted EM fields for various biomedical and nonbiomedical applications,[32,33] and are now considered as the "gold standard" for biomedical imaging numerical prediction and approximation. We present in Sec. 2 a description of the MC simulation used to derive the backscattered spatial Mueller matrices, starting from the skin tissue structural and dielectric model in Sec. 2.1 followed by a description of the calculation of the scattering coefficients of the embedded NPs and the choice of their properties in Sec. 2.2. We then briefly present the MC simulation scheme in Sec. 2.3 and the analysis procedure used to calculate the sensitivity of the backscattered field to the changes in tissue water content in Sec. 2.4. A discussion of the results is presented in Sec. 3, and a summary of the study is presented in Sec. 4.

2 Monte Carlo Simulation Details

In order to describe the MC simulation used here for assessing the products of THz polarimetric biomedical imaging, we provide in this section a description of the tissue model, NPs characteristics, MC algorithm, and results analysis method. Our MC simulation algorithm is based on the meridian plane MC algorithm presented and validated by Ramella-Roman et al.[34,35] for polarized light propagation and scattering, with adaptations for the stratified nature of the skin as has been described in Ref. 36 and widely implemented in many following works. For the sake of brevity, we therefore provide only a concise description for our MC simulation principles. Elaboration is provided regarding only modifications that we have introduced to the MC algorithm in order to accommodate for the structural and dispersive characteristics of the skin tissue at the THz, and for the scattering of EM fields from stratified spherical particles embedded in an absorbing medium. However, a detailed description is given in the following subsections regarding the skin tissue model (structural and dielectric properties), regarding the considerations in NPs selection and their properties and regarding the practical consideration of NPs insertion methods into the tissue, the resulting NPs distribution profiles in the skin and their resulting consequences for the sensitivity improvement sought in this work.

2.1 *Skin Structure, Electrical Properties, and Modeling*

Human skin is a very complex organ both in structure and physical behavior, due to the various functions it performs as the mediator between the inner tissues and the surrounding medium.[16] Skin tissue's complexity is a major challenge for the establishment of an accurate numerical model intended for simulating the interaction of EM fields with the skin tissue, which is the base of any numerical estimation for skin tissue imaging and biosensing numerical simulations. Thus, some simplifications to the structure of the skin and its electrical properties have to be made in order to establish a reasonable yet feasible model for numerical description of EM waves propagation. The nature of these simplifications varies with the considered EM spectral domain.

The first simplification deals with the basic structure of the skin, focusing on the relatively long wavelengths of the submillimeter wavelengths and THz spectral domain. Skin tissue models for optical purposes that have proved to present high agreement between numerical modeling results and experimental measurements, are best suited for submillimeter and THz wavelengths spectral domain, often adopt the stratified nature of skin tissue and assume it to be composed of three optically homogeneous and optically isotropic and dispersive layers.[16,17,37–40] These layers correspond to the major layers of the skin: the stratum corneum (SC) with a thickness of 30 μm, epidermis with a thickness of 100 μm, and dermis with a thickness of 1350 μm.[37,41] This three layer structure is sandwiched between an ambient (air) and substrate (subcutaneous tissue) layers, constituting the spatial structure for the MC simulation illustrated in Fig. 1. It is important to mention that this homogeneous layer model neglects the scattering effects by various tissue organelles and surface roughness, yet it can serve as a valid first approximation, and has been widely done so, since scattering effects caused by organelles are not significant and less prominent at the long wavelengths of the THz domain. As this is the case, the homogeneous material approximation of the skin layers by dielectric mixing approaches and effective medium theories has been the basis for many theoretical studies and their experimental validations in the THz and submillimeter wave lengths, among the references.[16,39,41]

This last discussion brings us to the second simplification of the skin tissue that deals with the dielectric properties of the skin in the discussed spectral domain. Since THz radiation is very sensitive to the presence of water in the tissue, the dispersion model of each layer is dominated by its water content. As a result, the skin layers' complex permittivity is varied mostly by the water content of each layer, and can be thus characterized by a parametric model describing the skin layers' dielectric permittivity as a combination of the permittivities of water, blood,

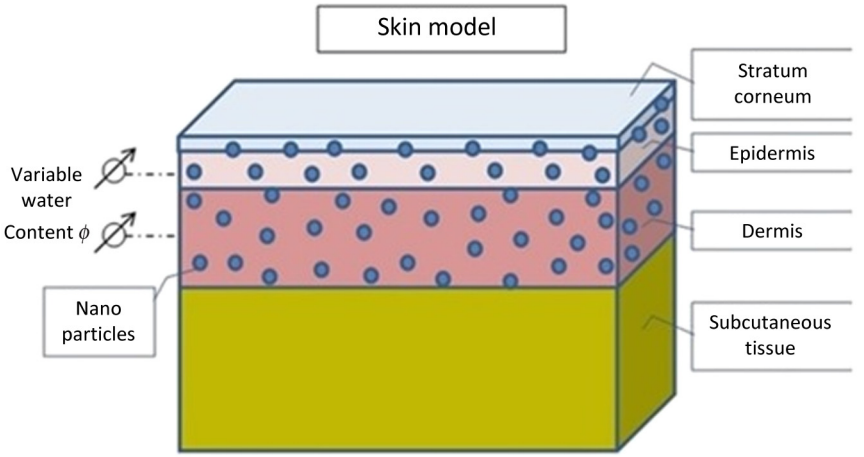

Fig. 1 Illustration of the stratified skin model embedded with nanoparticles (NPs) at the stratum corneum, epidermis, and dermis (with widths of 30 μm, 100 μm, and 1.35 mm accordingly) with variable values of the water content in the epidermis and dermis. NPs concentration in the different layers can be constant or decreasing with skin depth—depending on NPs insertion method (see Sec. 2.2).

and "dry biological material" as has been previously demonstrated[16,32,41] and based on experimental measurements at this spectral domain.[38,42–49] Similar parametric model approaches have been utilized to describe the effective scattering and absorption properties of skin tissue at the VIS and NIR.[50,51]

We apply a similar approach of dielectric mixing here in order to describe the dispersive dielectric behavior of the skin layers, based on experimental measurements and double Debye permittivity modeling based on THz pulse spectroscopy.[9,52] The basic idea is that the effective complex permittivity ε_{eff} of each layer can be described as a mixture of its constituents each having permittivity ε_i and a volume fraction of f_i, all obeying the dielectric mixing formula of the form presented in Eq. (1).[53] Here, the constituents of each layer are water, blood, and "dry biological matter" having the same complex permittivity in each layer but with different volume fractions

$$\sum_i f_i \frac{\varepsilon_i - \varepsilon_{\text{eff}}}{\varepsilon_i + 2\varepsilon_{\text{eff}}} = 0, \quad i \in \{\text{water}, \text{blood}, \text{dry bio matter}\}. \quad (1)$$

Since the complex permittivity of water and blood is known via spectroscopic measurements, we only need to determine the permittivity of "dry biological matter." The permittivity of the latter has been estimated to be 2.5 and with negligible losses at the lower portion of the THz wave region (up to 100 GHz), has not yet been determined for higher frequencies which are of interest to us, leaving only the above used low frequency permittivity for verification of a more wide frequency estimation described hereafter. We use the permittivity of the epidermis at THz frequencies determined by dielectric spectroscopy at THz frequencies[9,53] and extract the desired permittivity of "dry biological matter" from Eq. (1) based on the estimated volume fractions of water, blood, and "dry biological matter"[50] detailed in Table 1 for the epidermis. We then use it to determine the permittivity of the other skin layers based on each layers volume fractions parameters (Table 1).

Based on the established above dispersion model and by switching the notation for water and blood content (volume fraction), the complex permittivity of each skin layer k can be designated by $\varepsilon_k(\omega, \phi_k, \rho_k)$ where ω stands for angular frequency, ϕ_k for water content in skin layer k (and ρ_k for the blood content in skin layer k ($k \in \{\text{SC}, \text{epidermis}, \text{dermis}, \text{subcutaneous tissue}\}$). It is through this dependence of the complex permittivity on tissue water content, that the sensitivity to water content changes can be determined numerically, by examining the corresponding changes to the nature of the EM field backscattered from the skin tissue. In essence, the water content of each skin layer can be varied independently by gradually changing its value relative to the "normal" or nonpathological state water content parameter designated by ϕ_k for each of the skin layers, imitating pathological processes which exhibit higher water content values compared with normal tissue. Equation (2) illustrates this simple description of water content relative change per skin layer, where $\delta\phi_k$ is a measure of the relative change compared with

$$\phi_{k,\text{modified}} = (1 + \delta\phi_k) \cdot \phi_k, \quad (2)$$

the normal water content parameter ϕ_k. Having established the structural and dielectric properties and the mechanism through which we will introduce the tissue's water content changes associated to skin cancer, we turn to describe the considerations concerning the NPs.

2.2 *Nanoparticles for Localized Surface Plasmon Resonance and Scattering Calculations*

The scattering cross section and absorption cross section of a spherical NP have been shown[46,47] to be inversely proportional

Table 1 Skin layers' parameters—thickness and volume fractions of water, blood, and "dry biological matter" for the complex permittivity model for each skin layer.

Skin layer name	Thickness (μm)	f_{water}	f_{blood}	$f_{\text{dry bio material}}$
Stratum corneum (SC)	30	0.05	0	0.95
Epidermis	100	0.2	0	0.8
Dermis	1350	0.6	0.04	0.36
Subcutaneous tissue	—	0.7	0.05	0.25

to $\varepsilon_p + 2\varepsilon_m$, where ε_p is the complex permittivity of the particle and ε_m is the complex permittivity of the particles' surrounding medium. It is because of this relation that a considerable elevation of the scattered radiation's sensitivity to delicate changes in the skin's dielectric properties (i.e., in ε_m) is achieved. When embedding the tissue with metallic NPs that present for some frequency a negative value for ε_p similar in magnitude to that of the positive value of $2\varepsilon_m$, a local maxima in the scattering and absorption cross sections is achieved. This spectral behavior is illustrated in Fig. 2 which presents the extinction cross section for InN, InSb, and Si both bare and coated with Parylene-C shell at the THz spectral domain. Figure 2 provides an intuitive explanation to the enhanced sensitivity to water content-induced dielectric (ε_m) changes by realizing that for a given frequency near that of the LSPR a change in ε_m causes a considerable change in the cross sections. This is due to the rapidly changing spectral pattern of the cross section with the changes in ε_m, causing a considerable relative change in the backscattered intensity. This relative change in intensity is expected to be much more significant than the one caused by the change in the permittivity without the presence of NPs.

Since the dielectric properties of the skin are a given reality, in order to achieve this high sensitivity at the spectral domain of interest, the obvious degree of freedom is the choice of the NPs' material. This choice must satisfy the condition that the NPs will present LSPR associated rapid changes in scattering and absorption cross sections in the spectrum domain of interest. Having presented the advantages of THz spectral domain for biomedical imaging, we examine InN, InSb, and highly doped Si as candidate materials for the desired NPs as they will present LSPR behavior in this spectral domain and will further improve its performance. However, the biocompatibility of the above materials is not clear in contrary to that of gold and silver used for LSPR-based biosensing at the visible domain, so a configuration InN/InSb/Si-based NPs with an outer layer that is biocompatible and biostable must be considered instead of pure InN/InSb/Si NPs. We consider InN/InSb/Si spherical particles coated with Parylene-C, a material which has been verified for biocompatibility, biostability, and thermal stability; and has been widely used for *in vivo* applications such as stents, cardiac assist devices, surgical tools, implants catheters, and other applications; and has been approved for use by the U.S. Food and Drug Administration and is compliant with ISO standards.[54–57] These NP configurations of Parylene-C coated InN/InSb/Si NPs could thus be considered safe for insertion into tissue. Parylene-C also possess dry-film lubricity allowing multilayer penetration[57] which is a desirable quality for the insertion process of the NPs into the skin tissue, since we are interested in sensing water content variations in the deeper skin layers (epidermis and dermis). Throughout this work, we maintain a Parylene-C coating width of 2 nm for all various core material radii.

2.2.1 *Scattering coefficients for coated and uncoated nanospheres embedded in absorbing media*

Propagating through the skin tissue or model, the EM field will experience scattering and absorption by the embedded NPs according to the scattering characteristics determined by Mie scattering formalism. These scattering properties, as have already been mentioned, are dependent both on the scatterers' properties and on the medium in which they are embedded in, as well as on the particles geometric properties. Embedding metallic NPs with different dispersive characteristics: InN,[31,52] InSb,[58] highly doped Si[59] (with free carrier concentration of $N_c = 5 \times 10^{19}$), Au,[60,61] and Parylene-C,[62] into the three skin layers having electrical properties presented in Sec. 2.1, leads to the less trivial case of Mie scattering formalism where both scatterers and surrounding medium have complex permittivities. We determine the scattering properties of the NPs by extending the algorithm described by Frisvad et al.,[63] the recursive algorithm presented by Pena and Pal[64] for the calculations of the scattering coefficients and cross sections for scatterers in absorbing media with the algorithm presented in Refs. 65 and 66 in order to allow for the treatment of coated spheres in absorbing medium. These scattering properties have then incorporated into the MC simulation, allowing calculating the scattering direction, amplitude, and polarization state of the backscattered field.

In order to strengthen the validity of the MC simulation predicted results, all of the scattering coefficients, cross sections,

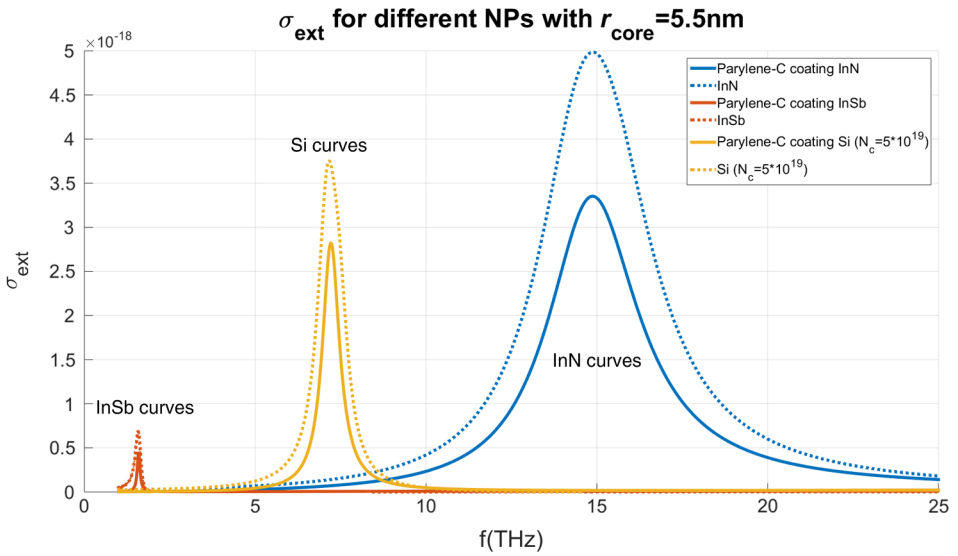

Fig. 2 Localized surface plasmon resonance dominated extinction cross section for InN, InSb, and Si and for Parylene-C coated InN, InSb, and Si NPs with core radius of 5.5 nm embedded in the epidermis at terahertz (THz) frequencies. The Parylene-C coating width is set as 2 nm.

asymmetry factor, and the Lorentz–Mie coefficients calculations integrated into our MC simulation have been compared with several different examples of uncoated and coated spherical particles of different materials embedded in a variety of surrounding mediums as have been presented in the literature.[47,63–66]

2.2.2 *InN nanoparticles properties determination for comparative studies*

The choice of NPs parameters such as radius and concentration must satisfy both the need for a significant extinction cross section and practical biomedical considerations. On the one hand, in order to yield a high impact on the reflected field pattern, we wish to maximize the effect of the NPs, i.e., maximizing the extinction coefficient described in Eq. (3), where V_0 is the volume fraction of NPs in the tissue, $V_{\text{single particle}}$ is the volume of a single particle, and σ_{ext} is the cross section of the NP

$$\mu_{\text{ext}} = (V_0/V_{\text{single particle}}) \cdot \sigma_{\text{ext}}. \tag{3}$$

We further demonstrate that, in Fig. 3, the extinction cross-section peak is directly proportional to the NPs radius; and in Fig. 4, the maximum change in the extinction cross section presents similar behavior. Figure 4 illustrates that InN and highly doped Si NPs are better than InSb; and since no considerable difference exists between InN and Si, we continue our work with the simpler InN material and set the frequency for $f = 14$ THz since it was demonstrated to give the highest change in the extinction cross section due to water content change as can be seen in Fig. 4.

It has been established that using larger NPs in a concentration as high as possible is expected to yield a high extinction cross section/coefficient which will lead to considerable variation with changes in ε_m. On the other hand, practical biomedical considerations might limit the size and concentration of the NPs, depending on the NPs insertion into the skin method, since the permeability of the intact tissue is inversely dependent on the particle size and too high concentration of particles in the tissue may obviously damage its functionality. Two common methods are considered for inserting the NPs into the skin: injection of NPs (local injection using a needle or needle free and systematic injection) or via an NPs solution that is applied to the skin's outer surface. The latter method introduces a limit on the size of the suggested InN NPs, even compared with the sizes of the traditional spherical NPs used in biomedical optics in the visible and NIR spectrum which are made of gold or silver and usually have radii of 50 nm[15] or less,[66] and has severe implications on the applicability of the NPs-based sensitivity enhancement method sought here.

Both considered NPs insertion techniques, injecting the NPs into the skin or applying them on the skin's outer surface and letting them diffuse into the skin, are expected to result in different NPs distribution and concentration profiles in the tissue. The insertion method via the external application of a solution of NPs in some aqueous material has been widely studied and it has been recently demonstrated that gold and silver NPs that have been prepared properly can penetrate the outer skin layer, the SC, and reach the deeper skin layers[67–70] but with decreasing concentration. Furthermore, it has been demonstrated[61,68,70] via transmission electron microscopy, two photon photoluminescence microscopy, and a sectioning imaging technique suggested by Labouta et al.[68,71] enabling to quantify the number of NPs in the skin samples, that the penetrability of the intact healthy skin to NPs is inversely proportional to the NPs' radii, and directly proportional to the NPs' concentration in the applied solution and skin exposure time to the solution. We adopt the particle core radii (3 and 7.45 nm as larger NPs do not penetrate efficiently the SC), NPs concentrations in the solution and skin exposure time (24 h) provided in Ref. 68 in order to credibly model the skin penetration/volume fraction profile of the Parylene-C coated InN NPs with equal dimensions. We then fit these measured values to exponentially decreasing profiles of the form $V(z) = V_0 \cdot e^{-a*z}$ and insert it into the MC simulation as the distribution of NPs concentration across the skin tissue. Yet, since the MC simulation can manage only a fixed value of NPs concentration in a specific layer, we divide the epidermis and dermis layers into sublayers each with a thickness of 50 μm having a constant concentration of NPs. It is important to stress that the immersion of NPs in an aqueous solution does not

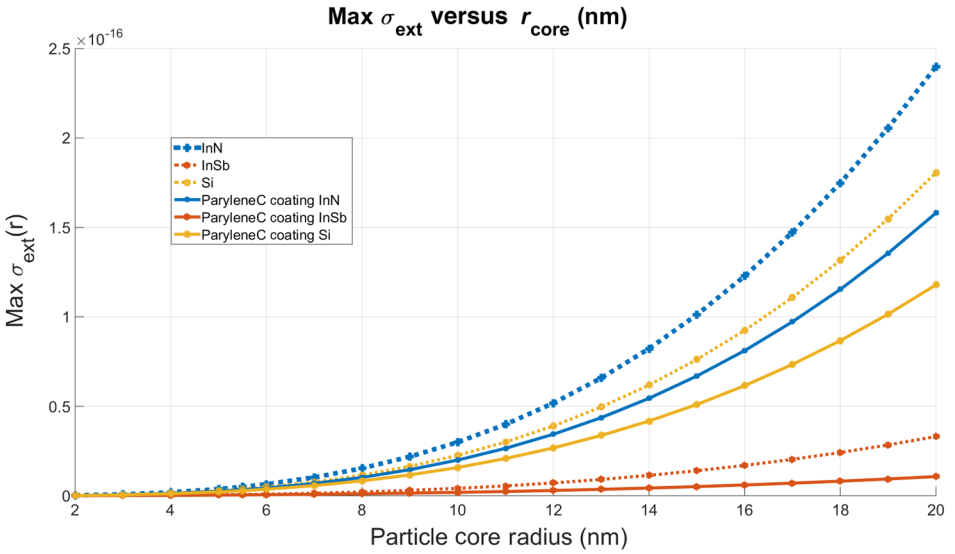

Fig. 3 Peak value at THz frequencies of the extinction cross section for bare InN, InSb, and Si NPs and for coated ones with Parylene-C shell embedded in the epidermis versus core radius. A clear rise in peak extinction cross section is seen with increasing particle radius.

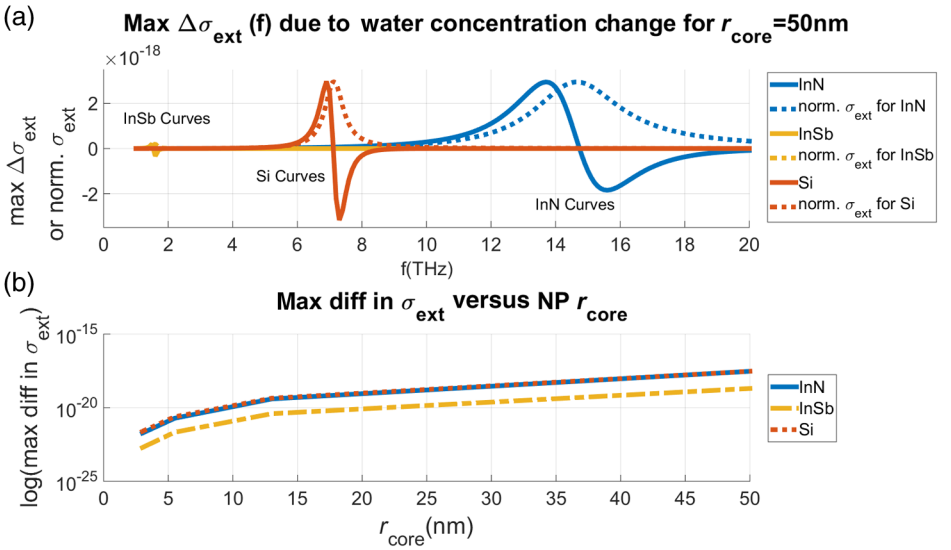

Fig. 4 Maximum change in the extinction cross section. (a) Change in extinction cross section versus frequency due to a relative change of 1% in water content and normalized extinction cross section pattern for normal water content for Parylene-C coated InN, InSb, and Si NPs embedded in the epidermis with core radius of 50 nm. Maximal change in cross section is achieved at a lower frequency than the one for maximal cross section for initial water content. (b) The maximal change of the extinction cross section versus particle core radius for Parylene-C coated InN, InSb, and Si NPs embedded in the epidermis. A clear rise in maximal change with particle radius is visible (notice logarithmic *Y*-axis).

change the water content of the tissue, which might have affected the water content-based detection of relative and localized changes in the skin, as after a long exposure time to the solution the aqueous part easily diffuses away into the skin, spreads in it, and vanishes. At this point, it is worth addressing that the NPs solutions described in Ref. 68—3 nm particles with low and higher initial concentration in the solution and a 7.5 nm particles with low concentration in the solution yield low NPs concentrations depositions in the skin which rapidly decay in magnitude as the skin deepens. The description of the sensitivity improvement results based on this approach of NPs insertion are described in Sec. 3.

The second insertion method via injection on the other hand appears to result in a relatively uniform concentration of particles in each layer since it has low dependence on skin tissue permeation mechanisms because the injection process bypasses the SC layer which functions as the main barrier set to prevent the NPs from penetrating from outside the skin. Two different approaches for injecting the NPs into the skin exist in the literature. The first is a local injection or multiple close injections of an aqueous solution with NPs either by a needle or by needle-free technique[72] meant to bypass the SC and directly insert the NPs, with radii up to ~340 nm,[72] into the epidermis and dermis at high concentrations. The second is a systematic injection of an aqueous solution with NPs where a high concentration solution is injected into the vein and spreads out through the body.[73] Some of the NPs reaches and permeates into the skin tissue from within the blood vessels that supply the skin with vitals. This approach has been recently studied in mice and has surprisingly been shown to be nontoxic even at dosages that were enough to accumulate in the skin in a manner visually detectable. In this approach, our NPs distribution is uniform in the epidermis and dermis, yet no NPs are introduced into the SC and only negligible amount of NPs is expected to permeate into the SC from the epidermis as can be intuitively deduced from the results of the first approach.

In order to study the sensitivity improvement dependence on NPs radii and volume fraction distribution in the tissue, we simulate the reflectance patterns for both insertion methods, and for five different values of NPs core radii: 3, 7.5, 15, 50, and 150 nm with different concentration profiles according to the insertion methods. All radii values are used to examine the detection sensitivity improvement expected by the second insertion method for three different uniform concentrations in the skin. The first two radii values are used for the first insertion method and for three profiles based on the data from Ref. 68 and one elevated volume fraction profile based on data extrapolation. The latter has been performed in order to assess the effect of applying a very high concentration solution of NPs to the outer layer of the skin. The radii and volume fraction parameters used for the different simulations are summarized in Table 2.

2.3 *Monte Carlo Simulation Scheme*

The MC simulation follows the position, polarization state (Stokes vector), and intensity of each of the photons as they propagate through the stratified structure, experiencing sequential scattering events by NPs and skin layer boundary interactions. These interactions continue until the photons have either decayed in intensity below a predetermined threshold, transmitted into the substrate (absorbed by the structure) or emitted back out of the structure at the interface between the ambient and first skin layer, thus contributing to the reflected radiation. The unique concatenation of scattering events, boundary interaction and propagation between them, including rotation matrices to and from the polarization reference planes, shape the accumulated Mueller matrix for each photon describing the relation between the Stokes vectors of each photon from the normal-incident narrow pencil beam to the Stokes vector of the reflected photon. The incoherent spatial sum of the reflected photons' Mueller matrices, or "Mueller matrix maps," is the output of the MC simulation[34,35,74,75] and the basis for the sensitivity

Table 2 Nanoparticles (NPs') parameters and volume fraction profiles for both insertion methods considered.

Insertion method 1—permeation into the skin through the SC				
Profile name	3 nm—low	3 nm	3 nm—high (extrapolated)	7.5 nm—low
Particle core radius (nm)	3	3	3	5.5
NPs volume fraction profile	$5.987\times10^{-9}\cdot e^{-87.819\times10^{3}z}$	$6.297\times10^{-9}\cdot e^{-39.819\times10^{3}z}$;	$6.2978\times10^{-7}\cdot e^{-397.72\cdot z}$	$1.5156\times10^{-9}\cdot e^{-35.545\times10^{3}z}$

Insertion method 2—injection (local or systematic)					
Particle core radius (nm)	3	7.5	15	50	150
NPs volume fraction at SC (constant)	0	0	0	0	0
NPs volume fraction at epidermis (constant)	10^{-4}, 10^{-5}, 10^{-6}				
NPs volume fraction at dermis (constant)	10^{-4}, 10^{-5}, 10^{-6}				

analysis. It should be noted that even though there is no difference between the outcomes of MC simulations of polarized light propagation and scattering that are based on Jones or on Mueller analysis,[74,75] we have selected Mueller analysis since it is more common and therefore intuitive for analysis, although our simulation also gathers the Jones matrix and the Jones matrix data for coherent backscattering (CBS) as described in Refs. 76–78. Validation of the generated Jones matrix patterns and the CBS patterns against results from the literature for different tissue configurations strengthen the validity of the used MC simulation.

The MC simulation logical scheme is based on the meridian plane MC simulation for polarized light propagation and scattering presented by Ramella-Roman et al.[34,35] Modifications to the logic and scattering calculations have been made only to support the nature of the particles discussed in Sec. 2.2. However, in order to accommodate for the skin layered structure, considerable modifications to the logical scheme presented in Ref. 34 have been made based on the widely adopted principles of "Monte Carlo model of steady-state light transport in multi-layered tissues" simulation for light scattering in multilayered media as have been presented in Ref. 78 now fitted to treat scattering of polarized light in multilayered structures. The logical scheme for our simulation is presented in Fig. 5, which is followed by a short explanation of some of the main stages in the scheme.

Launch new photon—Each new photon is initialized and is given initial values for its direction, its Stokes vector, its position in the cross section of the beam according to the beam's shape and incidence angle and an initial weight of unity. Here, a normal-incident pencil beam shape was set propagating initially in the positive z direction.

Propagate to interface/scatterer—Each photon is moved along the propagation (phase) direction until it reaches an interface or a scatterer according to the next interaction type. The photon's weight is updated by an exponential intensity decay factor due to propagation in medium with dielectric losses.

Interface—Based on the incidence angle of the photon and the complex permittivity of the mediums on both sides of the interface, the reflection, and transmission coefficients and the suitable interface interaction Jones and Mueller matrix[79] are calculated. The photon is either reflected or transmitted through the boundary according to a selection process similar to the one presented in Ref. 78.

Determine next interaction type—While the photon is within the skin model, it can either experience an interaction with an

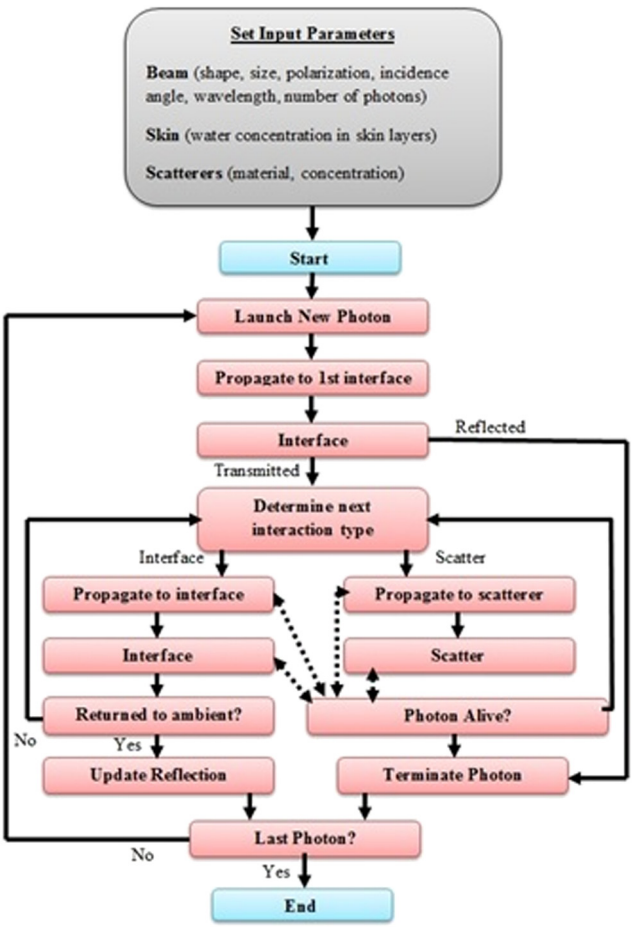

Fig. 5 Logical scheme of the Monte Carlo simulation for the stratified skin model embedded with NPs. The detailed description of the stages is given in Sec. 2.3.

interface between two skin layers or a scattering interaction with an NP. The decision on which of the two interaction types is done similarly to the principles described in Ref. 79.

Scatter—The polar θ' and azimuthal ϕ' scattering angles are determined for each scattering event by a rejection method similar to the one described in Ref. 34 (but with properly normalized pdf). When a set of angles is selected, the photon direction is updated to match the scattering angles and the interaction matrix is determined by the selected angles θ', ϕ' as described in Ref. 34. A change of photon's intensity is made only in the case that the absorption cross section does not vanish. This is done by multiplying the photon's Stokes vector, interaction Mueller matrix, and photon weight by a factor of the well-known albedo ($\sigma_{\text{scat}}/\sigma_{\text{ext}}$) which is the relation of the scattering and the extinction cross sections.

Photon alive?/terminate photon/update reflection—After each propagation, scattering, and interface event, the photon's position is examined; and the intensity weight of the photon is compared with a predetermined value in order to determine if the photon's intensity has not dropped enough to proclaim the photon as "dead" and abandon it. While the photon is not "dead," the logical flow of the photon in the simulation continues until either the photon is transmitted into the subcutaneous tissue and terminated or is reflected from the skin model into the ambient and is collected by the sensor—contributing to the reflectance. Each of the collected photons' Mueller matrix is incoherently added to a spatial Mueller matrix or Mueller matrix map, according to the position in which the photon was emitted back to ambient, after rotating the reference frame of the photon's accumulated Mueller matrix to that of the sensor's which are the original XYZ axes.[34]

A demonstration of the normalized Mueller matrix map of the reflected radiation for two cases can be seen in Figs. 6 and 7. The first one, illustrated in Fig. 6, is a successful sanity check for the MC simulation for the simple case of polarized light at the visible domain propagating in and scattered by a homogeneous dilution of polystyrene spherical NPs in water, which became a common test case for MC simulations, and can be used for comparison between different MC simulations and to the results of a simple experimental setup.[36,37,80]

Figure 7 illustrates the Mueller maps for the skin model embedded with Parylene-C coated InN NPs. It can be seen that the spatial patterns are similar to the case of polystyrene NPs embedded in water, yet they are less prominent due to both absorption by the skin layers and the particles themselves, and due to the reflection and refraction effects that arise due to the stratified structure of the skin.

2.4 *Analyzing the Mueller Maps*

Several iterations with 10^7 photons each of the MC simulation for the skin structure embedded with Parylene-C coated InN NPs were performed for the volume fraction profiles and radii discussed in the previous sections and summarized in Table 2. Each iteration was made with a slightly increased value of the water concentration (up to 0.5% change) in the epidermis and dermis layers, typical for melanoma and basal cell carcinoma (BCC) which manifests themselves at these skin layers.[80] Gathering and examining the Mueller maps resulting from the different iterations, one can determine that they differ from each other by some small change of the spatial pattern of each of the Mueller matrix elements. A comparative study was performed in order to evaluate the relative change between the maps, caused by the changes in the water content of the skin layers.

Since dealing with spatial patterns, the first and intuitive approach is to compare each Mueller map simulated for elevated water content to that of the original having "normal" water content, and assign a measure to the relative change between them using a grade quantifying their difference. Such a grade can be a root mean square error (RMSE) grade for each Mueller map element. Though this approach does indeed present a monotonous rise in this RMSE grade as the relative change in water content increases, this approach is less immune to errors due

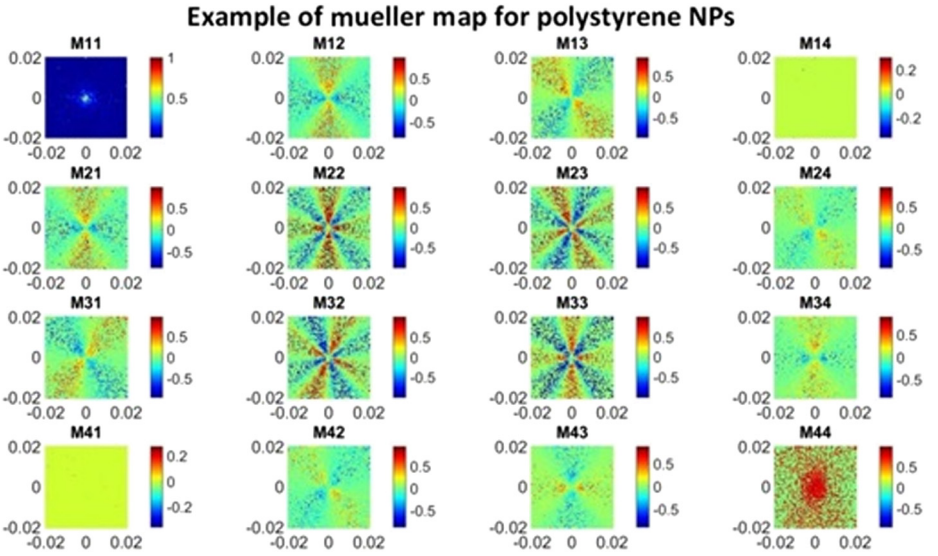

Fig. 6 Normalized spatial patterns of the Mueller matrix maps for a monodispersed solution of polystyrene NPs of 2.02 μm in diameter in water examined by a narrow pencil beam at 534 nm similar to the simulated and experimental results given by Ramella-Roman et al.[35] Prominent spatial patterns are demonstrated for all Mueller matrix elements except M41 and M14. The horizontal and vertical scales are in centimeters.

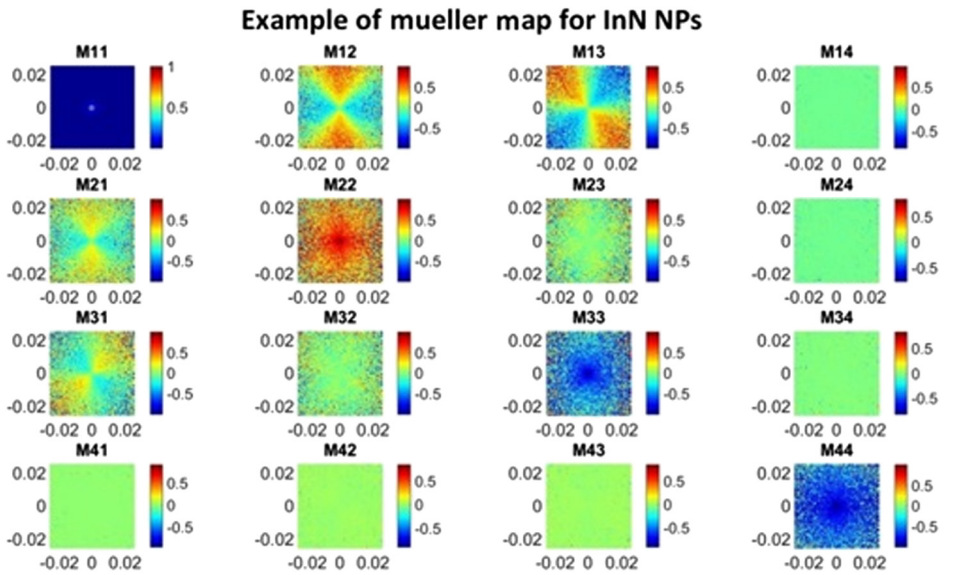

Fig. 7 Normalized spatial patterns of the Mueller matrix maps for InN NPs in the skin model. Less prominent spatial patterns are demonstrated relative to the case of the no absorption case of the polystyrene spheres in water due to the presence of absorption, both by the skin itself and by the particles as well as due to the interactions with the skin layers. The horizontal and vertical scales are in centimeters.

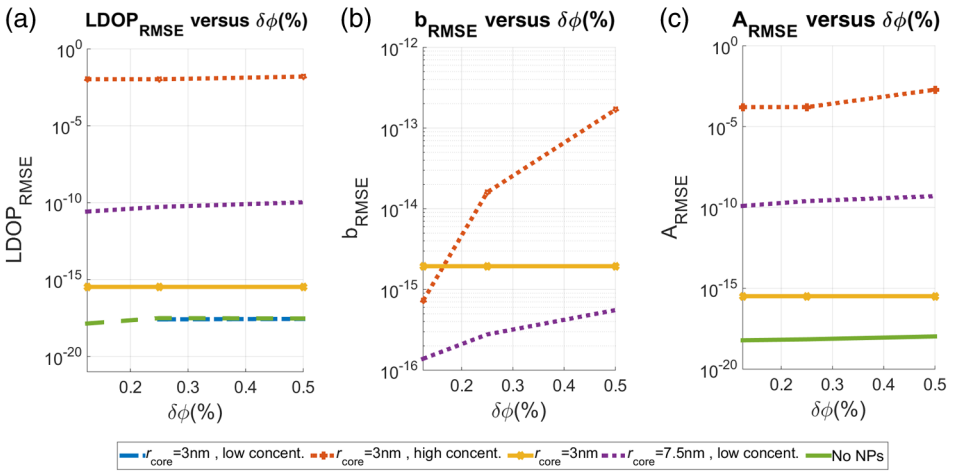

Fig. 8 Illustration of the root mean square error (RMSE) grade for (a) linear degree of polarization (LDOP), (b) *b*, and (c) *A* as a function of water content change in percentages, for skin without NPs and skin embedded with Parylene-C coated InN NPs inserted via permeation through the skin. NPs with radii of 3 nm for three different solution concentrations and 7.5 nm with the corresponding volume fraction profiles from Table 2 are presented. Note that *y*-axis is in logarithmic scale, RMSE grade values tending toward 0 or equal to it are omitted from the plots due to the logarithmic scale.

to the statistical nature of the MC simulation that is used to generate the data set. We have thus adopted and examined several polarimetric measures that can be expressed by combinations of the Mueller matrix elements M_{ij} ($i, j \in \{1,2,3,4\}$), thus having more "noise" immune mathematical expressions, and that have been demonstrated in the visible wavelengths domain both experimentally and numerically[19,20,25] to be efficient as polarimetric-based methods for contrast-based cancer detection. The polarimetric measures are the linear degree of polarization (LDOP) defined in Eq. (4) and the Mueller matrix transformation technique's measures b and A defined in Eqs. (5) and (6)

$$\mathrm{LDOP} = \frac{M_{21} + M_{22}}{M_{11} + M_{12}}, \tag{4}$$

$$b = \frac{M_{22} + M_{33}}{2}, \tag{5}$$

$$A = \frac{2 \cdot (M_{22} + M_{33}) \cdot \sqrt{(M_{22} - M_{33})^2 + (M_{23} + M_{32})^2}}{(M_{22} + M_{33})^2 + (M_{22} - M_{33})^2 + (M_{23} + M_{32})^2}. \tag{6}$$

The polarimetric measures LDOP, b, and A have been linked, in the visible wavelengths domain where scattering of light in the tissue is very dominant, to the presence and variation of the nature of tissue scatterers such as collagen fibers and cell nuclei and organelles induced by skin cancer (specifically BCC[19,20])

but have not been linked to the induced variations in water content since visible light is less sensitive to these variations. As mentioned earlier, the longer wavelengths of the THz radiation cause significantly less scattering, thus the sensitivity of these parameters in THz to changes in the tissue scatterers will be much less and in our homogenized model even negligible rendering this skin cancer detection method useless. However, the introduction of NPs into the tissue that do have significant scattering and extinction properties via LSPR may revive the effectiveness of this detection method, but through the detection of skin cancer-induced water content changes and not tissue organelles variations. An analysis of the limit of detection based on these polarimetric measures is then performed in order to evaluate this suggested skin cancer detection methodology's sensitivity and usefulness.

We examined the relative change in the above polarimetric measures compared with relative increase in water content in order to determine the sensitivity of polarized light imaging to water content changes in a tissue embedded with the NPs (for the different configurations in Table 2) and compare them with the behavior of the tissue without NPs. Since the relative change incline for the above polarimetric measures is faster for the case with NPs than without them, then the NPs do indeed increase the sensitivity of this Mueller matrix-based imaging method due to water content changes that can be related to skin cancer. Furthermore, as different configurations of scatterers interact differently with the THz radiation and thus are expected to result in different sensitivities, a brief study is performed in order to determine the sensitivity's dependence on the particle configurations presented in Table 2.

Since our raw data are the Mueller maps, having 16 elements for the 16 Mueller matrix elements each spreading on an array of pixels, three new scalar relative change grades are defined based on the LDOP, b, and A polarimetric measures given in Eqs. (4)–(6). We note by $M_{i,j}^{m,n}(\delta\phi)(i,j\in\{1,2,3,4\})$ the m, n pixel of the Mueller map element representing the Mueller matrix element M_{ij} resulting from the MC iteration with water content change by an amount of $\delta\phi$ (given in percentages relative to the "normal" initial value). The definitions in Eqs. (4)–(6) were then used to create the LDOP, b, and A maps by applying the relations in Eqs. (4)–(6) per pixel. Now we have as a result three new maps instead of the 16 of the Mueller maps, hereafter noted as $\mathrm{LDOP}^{m,n}(\delta\phi)$, $b^{m,n}(\delta\phi)$, and $A^{m,n}(\delta\phi)$. In order to evaluate the change in the above new maps resulting from the water content increase $\delta\phi$, the difference maps of the elevated water content tissue were examined relative to the nonelevated case, e.g., $\Delta b(\delta\phi) = b^{m,n}(\delta\phi) - b^{m,n}(\delta\phi = 0)$. The RMSE, also known as root mean square deviation, between these each two maps is given by summing over the pixels of the squared value of the square of the difference map divided by the number of pixels yielding a scalar instead of a matrix, as is illustrated for b in Eq. (7). These RMSE grades for the LDOP, b, and A measures will

$$b_{\mathrm{RMSE}}(\delta\phi) = \sqrt{\frac{\sum_{m,n}[b^{m,n}(\delta\phi) - b^{m,n}(\delta\phi = 0)]^2}{N_{\mathrm{pixels}}}}, \tag{7}$$

serve as the relative change grade evaluate the sensitivity of these measures to the water content change.

A self-consistency check of the simulation was made, by calculating the relative difference between LDOP, b, and A maps extracted from different runs of the simulation with the exact same parameters in order to verify that the statistical nature of the simulation does not result in statistical error comparable with the difference between simulation runs with even slightly changed water content.

3 Results and Discussion

Examining the MC simulation results for the first method for the NPs insertion into the skin through permeation of NPs through the SC layer, we learn that less than 0.0005% of the photons were scattered even once. This means the dominant types of interactions for the THz photons were attenuation by the linear absorption and skin layer interface interactions (reflection and refraction), as scattering is clearly almost negligible. These results are well expected due to the overall low and exponentially decaying of the NPs' concentration with skin depth profile in the tissue as a result of the NPs insertion method. As the scattering is almost nonexistent, the introduction of NPs into the tissue has negligible effect on the sensitivity to water content change, a fact that is evident through the results presented in Fig. 8 for the polarimetric measures LDOP, b, and A. The lowest concentration of 3 nm NPs is almost identical in behavior to that of the tissue without NPs. For the 3 nm NPs, increasing the concentration of NPs does result in relative increase in the RMSE grades, yet the slope of the RMSE grades plotted relative to the change in water content is still very low, as well as are the values of the change themselves. It can also be seen that the 7.5 nm NPs have stronger reaction in LDOP and A to the water content change relative to the 3 nm with the low and moderate concentrations. This is due to the stronger scattering power of the larger NPs and the difference in the extinction cross section with increasing radii. Yet, the sensitivity of these parameters does not increase enough to be satisfying. Therefore, we examined the results for the second method of NPs insertion into the skin and neglected this insertion method.

The relative RMSE grade results for LDOP, b, and A measures estimated for water content changes up to 0.5% are presented in Fig. 9 for some of the injected Parylene-C coated InN NPs' configurations from Table 2, along with the RMSE grade results for similar simulation runs without the NPs. A clear monotonous rise in the RMSE grades can be noticed, indicating increasing difference between LDOP, b, and A maps for increasing water content. This desired monotonous behavior means that the NPs insertion into the skin has preserved the relationship between water content and reflected intensity of the EM fields enabling contrast-based imaging in THz to be used for the detection of water content change in the skin. Furthermore, the slope of the RMSE grade versus the relative water content change is a measurement of sensitivity of the polarimetric measures for changes in the water content: steeper rise means higher sensitivity to water content change. A clear improvement of sensitivity between the case without NPs and the case with NPs is evident, and sensitivity rises when the particle radius increases as might be expected. Before we turn to quantify the sensitivity of these RMSE grades to the water content change in the tissue, we notice that the values for the b measure are very low, thus implying low sensitivity to water content change. Therefore, this measure is neglected for the sensitivity improvement analysis that follows. It is also interesting to note that out of these same parameters, the LDOP and b measurements were more effective than A for detection of BCC in the visible wavelengths domain. For the THz wavelengths, however, b has become less

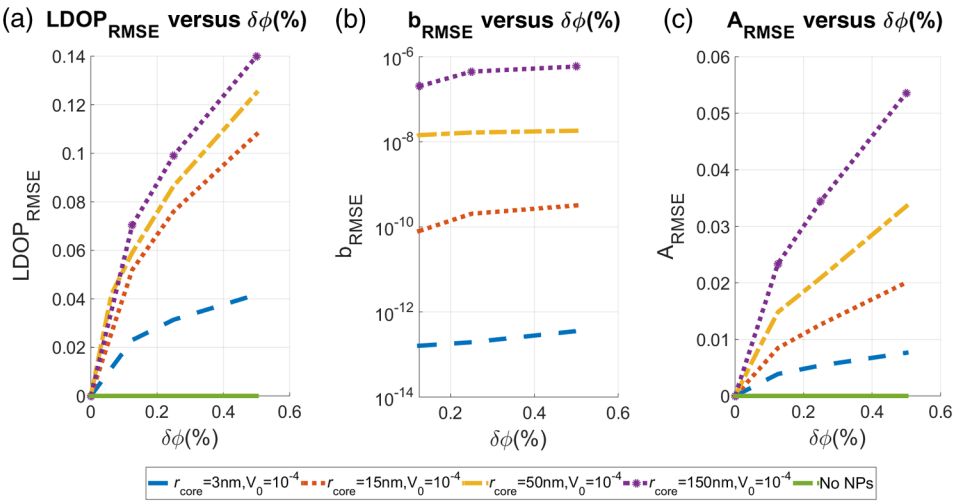

Fig. 9 Illustration of the RMSE grade for (a) LDOP, (b) *b*, and (c) *A* as a function of water content change in percentages, for skin without NPs and skin embedded with Parylene-C coated InN NPs with radii of 3, 15, 50, and 150 nm at a volume fraction of 10^{-4}. Monotonous rise in all RMSE grades is observed along with a significant improvement for the skin embedded with NPs. Note that the logarithmic *y*-scale for the *b* measure.

effective than *A* as the mechanism causing the variations has changed from variations in the particle sizes in the visible to the alterations of the particles' surrounding medium's complex permittivity that has stronger impact on the scattered field's spatial distribution. This impact results in breaking the isotropy of the overall scattered field distribution as the NPs number density is not that high as that of the cells and organelles, thus leading to lesser homogeneity of the scattered field distribution in the NPs embedded tissue.

Since Mueller matrix imaging is based on reflection measurements, the limit of differentiation (LOD) between skin tissue areas having slightly different reflection is limited by the repeatability of the reflection coefficient which is of the order of 0.001.[16,71] Comparing the relative change RMSE grades with the above repeatability value, one can estimate the LOD for each of the RMSE as is detailed in Eq. (8), where S is the slope of the considered RMSE grade around $\delta\phi = 0$ and $\langle\delta(\mathrm{RMSE})\rangle$ is the repeatability

$$\mathrm{LOD} = \frac{\langle\delta(\mathrm{RMSE})\rangle}{S}. \tag{8}$$

LOD values for LDOP and *A* RMSE grades and for each of the injected NPs configurations from Table 2 are detailed in Table 3. The lowest value for the considered configurations is $5.4 \times 10^{-3}\%$ achieved by LDOP for 150 nm NPs with a volume concentration of 10^{-4}. This lowest LOD is achieved for the largest NP considered and with the highest volume fraction considered. These two characteristics combined do not imply that the THz photons have gone through the greatest number of scattering events, as the extinction coefficient decays faster with particle radius than increases with extinction cross section. However, it means that the reflected intensity pattern has changed here mostly due to the scattering events that have occurred, because larger particles have larger change in the extinction cross section as have been illustrated.

For comparison, water content changes in malignant tissue can reach ~5% as has been demonstrated by various methods detailed in Ref. 81. Another interesting comparison is with the results of our earlier work,[16] where we have performed a similar analysis for the LOD% of water content change based on ellipsometric parameters using an analytic approach. It has deduced an LOD of 0.063% after performing frequency and incidence angle optimization which is not performed in this current

Table 3 Limit of detection for water content change for the polarimetric measures linear degree of polarization LDOP and *A* study as calculated from the relative change grade for InN coated with Parylene-C NPs.

NPs volume fraction	10^{-4}		10^{-5}		10^{-6}	
Polarimetric measure NPs core radius	LDOP (%)	*A* (%)	LDOP (%)	*A* (%)	LDOP (%)	*A* (%)
3 nm	0.0054	0.0322	0.0261	0.2318		
15 nm	0.0024	0.0148	0.0039	0.0435	0.0101	0.8896
50 nm	0.0021	0.0098	0.0037	0.0357	0.0091	0.6752
150 nm	0.0018	0.0054	0.0036	0.0296	0.00632	0.0626

study. The results presented here imply at least an order of magnitude improvement in the LOD by introducing the Parylene-C coated InN NPs with high enough extinction cross section (achieved by the high volume fraction of NPs in the tissue and the large radius of the NPs). Even better results might be achieved by optimization of particle size and concentration in the tissue, as at some point increasing the NPs radius should become inapplicable or just cause too few scattering events when maintaining constant volume fraction of particles in the tissue.

4 Summary

NPs that present LSPR in the THz wavelengths were suggested to be incorporated in tissue through two insertion methods in order to elevate the sensitivity to water content variations in the skin that have been associated with skin cancer. After evaluating several configurations of coated particles, Parylene-C coated InN has been selected as the best alternative for NPs configuration, presenting both high sensitivity to water content change and biocompatibility. The insertion method using injection of NPs into the skin by either localized or systematic injection has been analyzed via MC simulation, leading to the conclusion that the latter is preferable for *in vivo* methods as it provides the ability to insert NPs with larger dimensions and achieving higher concentration of NPs in the tissue, both needed for amplifying the NPs' effect. The insertion of NPs in the skin has been demonstrated to enable the use of the Mueller-based polarimetric imaging measures LDOP, b, and A, otherwise ineffective due to the low scattering effects in the THz wavelengths domain. The insertion approach by NPs permeation might be reconsidered for *ex vivo* examination, where the SC layer limiting the permeation into the deeper skin layers that are of interest, can be removed as is done widely in *ex vivo* methods.

Using a parametric analysis of the NPs concentrations and radii, it has been demonstrated that the limit of detection for water content changes in skin tissue, associated with several pathological conditions including skin cancer, can be lowered beyond previously estimated values[16] for tissues free of NPs. Thus, by performing Mueller matrix imaging at the THz wavelengths, the effect of LSPR sensitivity enhancement can lower the limit of detection to estimated changes in water content down to 0.0018 (%) for NPs with core radius of 150 nm and a high enough volume concentration. This configuration, out of the ones studied, already demonstrated an improvement of 1 order of magnitude relative to previously attained results based on ellipsometric measures.

It is important to note that better results might have been reached by another choice of incidence angle (oblique incidence), a different selection of frequencies and other configurations of NPs' size and concentration. Such optimization is required for maximization of sensitivity; however, it is very exhausting and time consuming with the means of MC simulation runs, especially for our MC simulation written in MATLAB environment. The results presented here are thus considered as a demonstration of a concept for LOD improvement, and such that enables polarimetric detection of skin cancer in THz, where skin EM response can be approximated rather accurately by homogeneous and isotropic models that render polarimetric analysis redundant under these approximations. As it has been demonstrated widely in the visible domain, polarimetric imaging and detection by polarimetric contrast analysis provides better, more accurate and sharper detection and localization of skin (and other) tumors.

Although no experimental validation of these results was performed, and the accuracy of MC simulations is limited, we can suggest with high confidence that within the accuracy scope of MC simulation a monotonous rise in the relative change parameter with increasing water content in the tissue does take place, and at much higher rate than the one without the NPs. This leads to the conclusion that InN, NPs, LSPR-based sensitivity enhancement for Mueller matrix imaging is worth further examining for biomedical sensing and also for other THz sensing applications as well. Our hope is that this study will initiate a discussion and attempts to perform experiments to verify the theoretical predictions.

References

1. B. Kunnen et al., "Application of circularly polarized light for non-invasive diagnosis of cancerous tissues and turbid tissue-like scattering media," *J. Biophotonics* **8**, 317–323 (2015).
2. R. Samatham, K. Lee, and S. L. Jacques, "Clinical study of imaging skin cancer margins using polarized light imaging," *Proc. SPIE* **8207**, 82070O (2012).
3. S. L. Jacques, J. C. Ramella-Roman, and K. Lee, "Imaging skin pathology with polarized light," *J. Biomed. Opt.* **7**(3), 329–340 (2002).
4. E. Du et al., "Mueller matrix polarimetry for differentiating characteristic features of cancerous tissues," *J. Biomed. Opt.* **19**(7), 076013 (2014).
5. S. L. Jacques et al., "Polarized light camera to guide surgical excision of skin cancers," *Proc. SPIE* **6842**, 68420I (2008).
6. M. Y. Sy et al., "A promising diagnostic method: terahertz pulsed imaging and spectroscopy," *World J. Radiol.* **3**(3), 55–65 (2011).
7. C. B. Reid et al., "Accuracy and resolution of THz reflection spectroscopy for medical imaging," *Phys. Med. Biol.* **55**(16), 4825 (2010).
8. E. Pickwell et al., "In vivo study of human skin using pulsed terahertz radiation," *Phys. Med. Biol.* **49**(9), 1595 (2004).
9. E. Pickwell et al., "Simulating the response of terahertz radiation to basal cell carcinoma using ex vivo spectroscopy measurements," *J. Biomed. Opt.* **10**(6), 064021 (2005).
10. R. M. Woodward et al., "Terahertz pulse imaging of ex vivo basal cell carcinoma," *J. Invest. Dermatol.* **120**(1), 72–78 (2003).
11. V. P. Wallace et al., "Terahertz pulsed spectroscopy of human basal cell carcinoma," *Appl. Spectrosc.* **60**(10), 1127–1133 (2006).
12. C. Yu et al., "The potential of terahertz imaging for cancer diagnosis: a review of investigations to date," *Quant. Imaging Med. Surg.* **2**(1), 33 (2012).
13. R. M. Woodward et al., "Terahertz pulse imaging in reflection geometry of human skin cancer and skin tissue," *Phys. Med. Biol.* **47**(21), 3853 (2002).
14. S. Fan et al., "The growth of biomedical terahertz research," *J. Phys. D: Appl. Phys.* **47**, 374009 (2014).
15. W. Cai et al., "Applications of gold nanoparticles in cancer nanotechnology," *Nanotechnol. Sci. Appl.* **1**, 17 (2008).
16. M. Ney and I. Abdulhalim, "Modeling of reflectometric and ellipsometric spectra from the skin in the terahertz and submillimeter waves region," *J. Biomed. Opt.* **16**(6), 067006 (2011).
17. M. Ney and I. Abdulhalim, "Does human skin truly behave as an array of helical antennae in the millimeter and terahertz wave ranges?," *Opt. Lett.* **35**(19), 3180–3182 (2010).
18. Z. D. Taylor et al., "THz medical imaging: in vivo hydration sensing," *IEEE Trans. Terahertz Sci. Technol.* **1**(1), 201–219 (2011).
19. H. He et al., "Mapping local orientation of aligned fibrous scatterers for cancerous tissues using backscattering Mueller matrix imaging," *J. Biomed. Opt.* **19**(10), 106007 (2014).
20. E. Du et al., "Mueller matrix polarimetry for differentiating characteristic features of cancerous tissues," *J. Biomed. Opt.* **19**(7), 076013 (2014).
21. B. Di Bartolo and J. M. Collins, Eds., *Biophotonics: Spectroscopy, Imaging, Sensing, and Manipulation*, Springer, Netherlands (2011).

22. J. Moan, "Visible light and UV radiation," in *Radiation at Home, Outdoors and in the Workplace*, D. Brune et al., Eds., Scandinavian Science Publishers, Oslo, Norway (2001).
23. J. Zhao et al., "Terahertz imaging with sub-wavelength resolution by femtosecond laser filament in air," *Sci. Rep.* **4**, 1–7 (2014).
24. H. T. Chen, R. Kersting, and G. C. Cho, "Terahertz imaging with nanometer resolution," *Appl. Phys. Lett.* **83**(15), 3009–3011 (2003).
25. E. Du et al., "Mueller polarimetry for the detection of cancers," *Proc. SPIE* **8935**, 89350S (2014).
26. F. Carmagnola, J. M. Sanz, and J. M. Saiz, "Development of a Mueller matrix imaging system for detecting objects embedded in turbid media," *J. Quant. Spectrosc. Radiat. Transfer* **146**, 199–206 (2014).
27. S. Demos, H. Radousky, and R. Alfano, "Deep subsurface imaging in tissues using spectral and polarization filtering," *Opt. Express* **7**(1), 23–28 (2000).
28. T. Novikova et al., "Contrast evaluation of the polarimetric images of different targets in turbid medium: possible sources of systematic errors," *Proc. SPIE* **7672**, 76720Q (2010).
29. Ó. Esteban et al., "Improved performance of SPR optical fiber sensors with InN as dielectric cover," *Proc. SPIE* **7753**, 77530X (2011).
30. Z. Sun et al., "A wide linear range surface plasmon resonance biosensor," *Proc. SPIE* **6047**, 604734 (2005).
31. A. Shetty, K. J. Vinoy, and S. B. Krupanidhi, "A study on the suitability of indium nitride for terahertz plasmonics," in *Proc. of the 2012 COMSOL Conf* (2012).
32. S. A. Prahl et al., "A Monte Carlo model of light propagation in tissue," *Dosim. Laser Radiat. Med. Biol.* **5**, 102–111 (1989).
33. B. L. Ibey et al., "Comparing finite difference time domain and Monte Carlo modeling of human skin interaction with terahertz radiation," *Proc. SPIE* **6854**, 68540Z (2008).
34. J. Ramella-Roman, S. Prahl, and S. Jacques, "Three Monte Carlo programs of polarized light transport into scattering media: part I," *Opt. Express* **13**(12), 4420–4438 (2005).
35. J. C. Ramella-Roman, S. A. Prahl, and S. L. Jacques, "Three Monte Carlo programs of polarized light transport into scattering media: part II," *Opt. Express* **13**(25), 10392–10405 (2005).
36. L. Wang, S. L. Jacques, and L. Zheng, "MCML—Monte Carlo modeling of light transport in multi-layered tissues," *Comput. Methods Programs Biomed.* **47**(2), 131–146 (1995).
37. G. Shafirstein and E. G. Moros, "Modelling millimetre wave propagation and absorption in a high resolution skin model: the effect of sweat glands," *Phys. Med. Biol.* **56**(5), 1329 (2011).
38. Y. Feldman et al., "The electromagnetic response of human skin in the millimetre and submillimetre wave range," *Phys. Med. Biol.* **54**, 3341–3363 (2009).
39. M. Saviz et al., "Theoretical estimations of safety thresholds for terahertz exposure of surface tissues," *IEEE Trans. Terahertz Sci. Technol.* **3**(5), 635–640 (2013).
40. C. Yu et al., "The potential of terahertz imaging for cancer diagnosis: a review of investigations to date," *Quant. Imaging Med. Surg.* **2**(1), 33 (2012).
41. S. Huclova, D. Erni, and J. Fröhlich, "Modelling and validation of dielectric properties of human skin in the MHz region focusing on skin layer morphology and material composition," *J. Phys. D: Appl. Phys.* **45**(2), 025301 (2012).
42. F. S. Barnes and B. Greenbaum, *Bioengineering and Biophysical Aspects of Electromagnetic Fields*, CRC Press, Boca Raton (2007).
43. P. S. Gabriel, R. W. Lau, and C. Gabriel, "The dielectric properties of biological tissues III. Parametric models for the dielectric spectrum of tissues," *Phys. Med. Biol.* **41**, 2271–2293 (1996).
44. W. J. Ellison, K. Lamkaouchi, and J. M. Moreau, "Water: a dielectric reference," *J. Mol. Liq.* **68**, 171–279 (1996).
45. R. Pethig, "Dielectric properties of body tissues," *Clin. Phys. Physiol. Meas.* **8**, 5–12 (1987).
46. S. R. Smith and K. R. Foster, "Dielectric properties of low-water-content tissues," *Phys. Med. Biol.* **30**, 965–973 (1985).
47. H. J. Liebe, G. A. Hufford, and T. Manabe, "A model for the complex permittivity of water at frequencies below 1 THz," *Int. J. Infrared Millimeter Waves* **12**, 659–675 (1991).
48. C. F. Bohren and D. R. Huffman, *Absorption and Scattering of Light by Small Particles*, John Wiley & Sons, New York (2008).
49. S. A. Maier, *Plasmonics: Fundamentals and Applications*, Springer Science & Business Media, New York (2007).
50. I. V. Meglinski and S. J. Matcher, "Quantitative assessment of skin layers absorption and skin reflectance spectra simulation in the visible and near-infrared spectral regions," *Physiol. Meas.* **23**(4), 741 (2002).
51. L. J. Steven, "Skin optics," http://omlc.org/news/jan98/skinoptics.html (1998).
52. E. Pickwell et al., "Simulation of terahertz pulse propagation in biological systems," *Appl. Phys. Lett.* **84**(12), 2190–2192 (2004).
53. S. Bosch et al., "Effective dielectric function of mixtures of three or more materials: a numerical procedure for computations," *Surf. Sci.* **453**(1), 9–17 (2000).
54. L. Wei et al., "Nano-/microtextured, free standing, flexible, thin film substrates of parylene C for cellular attachment and growth," *Mater. Res. Innovations* **16**(2), 84–90 (2012).
55. E. M. Schmidt, J. S. McIntosh, and M. J. Bak, "Long-term implants of Parylene-C coated microelectrodes," *Med. Biol. Eng. Comput.* **26**(1), 96–101 (1988).
56. Parylene Coating Services, "Conformal coatings for medical devices and the medical industry," http://www.paryleneinc.com/Parylene-Coatings-Medical.php (2011).
57. SCS Parylene Coatings, "Medical coatings," http://scscoatings.com/parylene-applications/medical-coatings (2014).
58. T. H. Isaac, W. L. Barnes, and E. Hendry, "Determining the terahertz optical properties of subwavelength films using semiconductor surface plasmons," *Appl. Phys. Lett.* **93**(24), 241115 (2008).
59. J. Grant et al., "Terahertz localized surface plasmon resonance of periodic silicon microring arrays," *J. Appl. Phys.* **109**(5), 054903 (2011).
60. Ace Learning Company, "OptiFDTD_80_Tech_Background_Tutorials," http://www.learningace.com/doc/624653/cbd72306e034651eef6b69937e1215c0/optifdtd_80_tech_background_tutorials (2014).
61. A. D. Rakić et al., "Optical properties of metallic films for vertical-cavity optoelectronic devices," *Appl. Opt.* **37**, 5271–5283 (1998).
62. M. Ji et al., "Study of parylene as anti-reflection coating for silicon optics at THz frequencies," in *Eleventh Int. Symp. Space THz Technology*, The University of Michigan, Ann Arbor, Michigan (2000).
63. J. R. Frisvad, N. J. Christensen, and H. W. Jensen, "Computing the scattering properties of participating media using Lorenz–Mie theory," *ACM Trans. Graphics* **26**(3), 60 (2007).
64. O. Pena and U. Pal, "Scattering of electromagnetic radiation by a multilayered sphere," *Comput. Phys. Commun.* **180**(11), 2348–2354 (2009).
65. P. Yang et al., "Inherent and apparent scattering properties of coated or uncoated spheres embedded in an absorbing host medium," *Appl. Opt.* **41**(15), 2740–2759 (2002).
66. I. W. Sudiarta and P. Chylek, "Mie-scattering formalism for spherical particles embedded in an absorbing medium," *J. Opt. Soc. Am. A* **18**(6), 1275–1278 (2001).
67. R. Fernandes et al., "Interactions of skin with gold nanoparticles of different surface charge, shape, and functionality," *Small* **11**(6), 713–721 (2015).
68. H. I. Labouta et al., "Mechanism and determinants of nanoparticle penetration through human skin," *Nanoscale* **3**(12), 4989–4999 (2011).
69. H. I. Labouta and M. Schneider, "Interaction of inorganic nanoparticles with the skin barrier: current status and critical review," *Nanomed. Nanotechnol. Biol. Med.* **9**(1), 39–54 (2013).
70. H. I. Labouta et al., "Combined multiphoton imaging-pixel analysis for semiquantitation of skin penetration of gold nanoparticles," *Int. J. Pharm.* **413**(1), 279–282 (2011).
71. http://www.sopra-sa.com/5-spectroscopic-ellipsometer-se-php.
72. C. H. Park et al., "Needle-free transdermal delivery using PLGA nanoparticles: effect of particle size, injection pressure and syringe orifice diameter," *Colloids Surf. B* **123**, 710–715 (2014).
73. E. A. Sykes et al., "Nanoparticle exposure in animals can be visualized in the skin and analysed via skin biopsy," *Nat. Commun.* **5** (2014).
74. H. Günhan Akarçay et al., "Monte Carlo modeling of polarized light propagation. Part I. Stokes versus Jones," *Appl. Opt.* **53**(31), 7576–7585 (2014).
75. H. Günhan Akarçay et al., "Monte Carlo modeling of polarized light propagation. Part II. Stokes versus Jones," *Appl. Opt.* **53**(31), 7586–7602 (2014).

76. A. Doronin et al., "Comparison of two Monte Carlo models of propagation of coherent polarized light in turbid scattering media," *Proc. SPIE* **8952**, 89520F (2014).
77. A. Doronin et al., "Two electric field Monte Carlo models of coherent backscattering of polarized light," *J. Opt. Soc. Am. A* **31**(11), 2394–2400 (2014).
78. A. J. Radosevich et al., "Open source software for electric field Monte Carlo simulation of coherent backscattering in biological media containing birefringence," *J. Biomed. Opt.* **17**(11), 115001 (2012).
79. H. Fujiwara, *Spectroscopic Ellipsometry: Principles and Applications*, John Wiley & Sons (2007).
80. M. J. Raković et al., "Light backscattering polarization patterns from turbid media: theory and experiment," *Appl. Opt.* **38**(15), 3399–3408 (1999).
81. National Cancer Institute, "Skin," http://www.cancer.gov/publications/patient-education/skin.pdf (2014).

Michael Ney is a PhD candidate in electro-optics engineering at the Ben-Gurion University of the Negev. He received his BSc degree in electrical engineering and BSc degree in physics from the Technion—Israel Institute of Technology in 2007 and received his MSc degree in electro-optical engineering from Ben-Gurion University of the Negev in 2011. His current research interests include biomedical imaging at the terahertz and submillimeter waves regions for skin cancer detection, polarized light imaging techniques, and Monte Carlo simulation methods. He is a member of SPIE.

Ibrahim Abdulhalim is a professor in the Department of Electro-Optic Engineering at Ben-Gurion University since 2005. His current research involves liquid crystal devices, nanophotonic and plasmonic biosensors, improved biomedical optical imaging techniques. He has published over 200 papers, 10 book chapters, coauthored two books and has over 15 patents. He is a fellow of the IoP and the SPIE. He is an associate editor of the SPIE *Journal of Nanophotonics*.